

# Laminarization Transition in Sediment-Laden Oscillatory Boundary Layers: A Computational Phase Map

Shmuel Link<sup>a)</sup>

Independent Researcher, Santa Cruz, California, United States

Wave-driven sediment transport models assume that turbulence persists in the oscillatory boundary layer, yet field and laboratory observations show that high suspended-sediment concentrations can suppress turbulence and trigger a laminar-like regime through a positive feedback in which stratification damps turbulent mixing, reducing vertical sediment diffusion and thereby reinforcing the stratification. We present a systematic computational study of this transition using a one-dimensional, vertically resolved model coupling momentum and sediment advection-diffusion with an algebraic stratification-damping closure. By sweeping the parameter space spanned by the Reynolds number  $Re$ , settling number  $S$ , and stratification parameter  $\Lambda$ , we produce a regime phase diagram mapping the transition topology  $\Lambda_c(Re, S)$ , which exhibits re-entrant boundaries where turbulence collapses at intermediate stratification but recovers at higher  $\Lambda$ . Because this critical surface depends on the adopted closure—here, an algebraic mixing-length model with linear Richardson-number damping— $\Lambda_c$  should be regarded as a model-specific phase boundary rather than a universal physical constant. Diagnostics include cycle-averaged turbulent viscosity ratio, drag coefficient, Reynolds stress, and phase-portrait attractor classification.

## I. INTRODUCTION

Oscillatory boundary layers driven by surface waves control the transport of sediment in coastal and continental-shelf environments. Standard engineering models assume fully turbulent conditions, parameterizing bed shear stress through empirical drag coefficients and eddy-viscosity closures. However, field measurements and laboratory experiments have demonstrated that sufficiently high suspended-sediment concentrations can stratify the boundary layer, suppress turbulent mixing, and trigger a transition to a laminar-like flow regime<sup>1–3</sup>. This laminarization alters effective drag, changes sediment flux scaling, and invalidates standard closures.

Despite repeated observations, and although partial regime mappings have been reported in DNS and LES studies<sup>2,4</sup>, no systematic, continuous parameter sweep spanning the full three-parameter space has been performed; existing DNS and LES studies provide regime classifications at discrete parameter points but do not map the complete  $(Re, S, \Lambda)$  surface. Existing studies report thresholds in terms of local parameters, but the regime space defined by the wave Reynolds number  $Re = U_0\delta/\nu$ , the settling number  $S = w_s/U_0$ , and the stratification parameter  $\Lambda = g\beta C_0\delta/U_0^2$  (the ratio of buoyancy forces from suspended sediment to oscillatory inertial forces) has not been swept continuously.

We address this gap computationally. By coupling the vertically resolved momentum equation with a sediment advection-diffusion equation and an algebraic turbulence closure damped by the gradient Richardson number, we sweep the  $(Re, S, \Lambda)$  parameter space to identify the critical surface  $\Lambda_c(Re, S)$  separating turbulent and laminar regimes. Although motivated by coastal sediment transport, the underlying stratification-turbulence interaction is generic, and the regime boundaries identified here may inform other stratified oscillatory shear flows, subject to the closure limitations discussed below.

## II. BACKGROUND AND PRIOR WORK

### A. Oscillatory boundary layers

The classical theory of oscillatory boundary layers originates with Stokes<sup>5</sup>, who derived the exact laminar solution for flow driven by a sinusoidally oscillating free stream above a flat plate. The solution reveals that viscous effects are confined to a thin layer of thickness  $\delta_s = \sqrt{2\nu/\omega}$ , the Stokes length, which serves as the fundamental length scale for all subsequent work on oscillatory boundary layers. This elegant analytical result remains the baseline against which turbulent oscillatory flows are compared<sup>6</sup>.

The transition from laminar to turbulent flow in oscillatory boundary layers has been investigated through a combination of experiment, linear stability analysis, and direct computation. von Kerczek and Davis<sup>7</sup> performed a linear stability analysis of the Stokes layer, establishing critical Reynolds number estimates for the onset of instability. Hino, Sawamoto, and Takasu<sup>8</sup>, Hino *et al.*<sup>9</sup> conducted pipe-flow experiments that identified a sequence of flow regimes with increasing Reynolds number: disturbed-laminar, intermittent-turbulent, and fully turbulent. Akhavan, Kamm, and Shapiro<sup>10,11</sup> carried out systematic experimental and numerical investigations of transition in bounded oscillatory flows, providing detailed measurements of the velocity field and Reynolds stresses through the transition process. On the fully turbulent side, the landmark experiments of Jensen, Sumer, and Fredsøe<sup>12</sup> measured velocity profiles and turbulence statistics at high Reynolds numbers over smooth beds, establishing benchmark data that have been widely used for model validation. Sleath<sup>13</sup> extended experimental investigations to rough beds, while Jonsson<sup>14</sup> developed wave friction factor relationships, and Grant and Madsen<sup>15</sup> formulated the widely used wave-current boundary layer model. The textbooks of Fredsøe and Deigaard<sup>16</sup> and Nielsen<sup>17</sup> synthesized much of this body of work into standard references for coastal boundary layer dynamics. The present study is restricted to hydraulically smooth beds; the additional complications in-

<sup>a)</sup>Electronic mail: sglink@gmail.com

troduced by bed roughness—including form drag and modified near-bed turbulence production—are beyond the present scope.

Numerical simulation has played an increasingly important role in elucidating the physics of oscillatory boundary layers. Spalart and Baldwin<sup>18</sup> performed early direct numerical simulations (DNS) of oscillatory wall-bounded flows. Vittori and Verzicco<sup>19</sup> used DNS to study transition mechanisms in detail, while Costamagna, Vittori, and Blondeaux<sup>20</sup> identified coherent structures and their role in turbulence production and transport. Salon, Armenio, and Crise<sup>21</sup> applied large-eddy simulation to the turbulent Stokes boundary layer, and Scandura<sup>22</sup> examined the structure of wall turbulence during the cycle. More recently, Özdemir, Hsu, and Balachandar<sup>23</sup> conducted DNS of smooth-walled Stokes layer transition, providing a detailed characterisation of the intermittent turbulence regime. Experimentally, Carstensen, Sumer, and Fredsøe<sup>24,25</sup> documented the formation and evolution of coherent structures and turbulent spots during transition, and Mier *et al.*<sup>26</sup> contributed further observations of transitional dynamics.

A common feature of nearly all of the studies cited above is that they consider clear-fluid oscillatory boundary layers, in which density is uniform and the turbulence dynamics are governed solely by shear. In many geophysical and engineering applications, however, the boundary layer carries suspended sediment whose concentration gradients introduce stable density stratification. The resulting interaction between turbulence, sediment transport, and buoyancy forces can fundamentally alter the transition process and even suppress turbulence entirely—a phenomenon broadly termed laminarization. Despite its practical importance, this coupled problem has received far less systematic attention than its clear-fluid counterpart, motivating the present investigation.

## B. Sediment stratification and turbulence suppression

Suspended sediment introduces a stable density stratification that opposes vertical turbulent mixing. The competition between stabilizing buoyancy and destabilizing shear is quantified by the gradient Richardson number,  $Ri_g = -(g/\rho)(\partial\rho/\partial z)/(\partial u/\partial z)^2$ . Miles<sup>27</sup> and Howard<sup>28</sup> established that  $Ri_g > 1/4$  everywhere is a necessary condition for the stability of an inviscid stratified shear flow, a result that underpins all subsequent turbulence damping criteria. The foundational treatment of buoyancy effects in turbulent flows is given by Turner<sup>29</sup>; more recently, Ivey, Winters, and Kos-  
eff<sup>30</sup> reviewed the subtle relationship between stratification, turbulence, and irreversible mixing.

A well-known limitation of  $Ri_g$ -based closures arises in oscillatory flows, where the mean shear  $\partial u/\partial z$  passes through zero twice per cycle. Near these flow-reversal phases the instantaneous  $Ri_g$  becomes singular or extremely large, even though the flow may remain dynamically unstable due to residual turbulent kinetic energy and finite-amplitude perturbations. This phase-dependent singularity complicates any closure that relies on the local, instantaneous Richardson number and motivates caution in interpreting cycle-phase-

resolved results.

Observational and experimental evidence for sediment-induced stratification effects has accumulated over several decades. Trowbridge and Kineke<sup>31</sup> documented fluid-mud dynamics on the Amazon continental shelf, where high near-bed sediment concentrations created strong density gradients that suppressed turbulent momentum transfer. Friedrichs *et al.*<sup>32</sup> showed that fine-sediment accumulation in coastal seas is closely linked to boundary-layer stratification processes, and Wright and Friedrichs<sup>33</sup> reviewed gravity-driven transport on continental shelves, emphasizing the role of wave-supported fluid muds. Winterwerp<sup>1,34</sup> systematically examined stratification effects across a wide range of sediment concentrations, from dilute non-cohesive suspensions to dense cohesive muds, identifying concentration thresholds beyond which turbulence is effectively quenched. Lamb, D'Asaro, and Parsons<sup>3</sup> measured the turbulent structure of high-density suspensions formed under waves, providing direct evidence of damped Reynolds stresses at elevated concentrations. Dohmen-Janssen<sup>35</sup>, Dohmen-Janssen *et al.*<sup>36</sup> documented grain-size-dependent phase lags and transport rates in oscillatory sheet flow, highlighting the role of vertical sediment distribution in controlling near-bed dynamics.

Direct numerical simulations have clarified the underlying mechanisms. Cantero, Balachandar, and Parker<sup>4</sup> simulated stratification effects in sediment-laden turbulent channel flow, demonstrating progressive turbulence suppression as the concentration—and hence the bulk Richardson number—increased beyond a critical level. Cantero, Shringarpure, and Balachandar<sup>37</sup> extended this work toward universal criteria for turbulence suppression in dilute turbidity currents. Most directly relevant to the present study, Ozdemir, Hsu, and Balachandar<sup>2</sup> performed DNS of fine-particle-laden oscillatory channel flow and showed that particle-induced density stratification can fundamentally alter the flow regime, driving a transition from fully turbulent to an intermittent or laminar-like state. Ozdemir, Hsu, and Balachandar<sup>2</sup> observed relaminarization at bulk Richardson numbers of  $O(10^{-2}-10^{-1})$ , which is broadly consistent with the critical  $\Lambda_c$  values found in the present study; however, direct quantitative comparison is complicated by differences in the turbulence treatment (DNS versus algebraic closure). In a broader context, relaminarization phenomena across fluid mechanics were reviewed by Narasimha and Sreenivasan<sup>38</sup>; more recent examples in non-sediment contexts include the pulsatile pipe flow experiments of Greenblatt and Moss<sup>39</sup> and the transient channel flow study of He and Seddighi<sup>40</sup>. Flores and Riley<sup>41</sup> used DNS to analyze turbulence collapse in the stably stratified surface layer. Balachandar and Eaton<sup>42</sup> provided an extensive review of turbulent dispersed multiphase flows, including two-way coupling effects relevant to particle-laden boundary layers.

Despite this body of work, a systematic mapping of the transition from turbulent to laminar-like conditions as a function of the governing dimensionless groups—the Reynolds number  $Re$ , settling number  $S$ , and stratification parameter  $\Lambda$ —has not been undertaken. Existing studies identify thresholds in terms of local parameters for specific flow configura-

tions, but no unified phase diagram delineates the critical stratification  $\Lambda_c(Re, S)$  at which turbulence collapses in oscillatory boundary layers. The present study addresses this gap through a comprehensive computational sweep of the  $(Re, S, \Lambda)$  parameter space.

### C. Turbulence closures for stratified boundary layers

The simplest algebraic turbulence closure is the Prandtl mixing-length model<sup>43</sup>, which prescribes the eddy viscosity as  $v_t = \kappa^2 z^2 |\partial u / \partial z|$ , where  $\kappa \approx 0.41$  is the von Kármán constant and  $z$  is the distance from the wall. Van Driest<sup>44</sup> introduced an exponential damping factor to enforce the correct near-wall scaling in the viscous sublayer. Despite its simplicity, this algebraic closure remains widely used in boundary-layer studies where the turbulence structure is well characterised by a single length scale. More sophisticated approaches include the  $k-\varepsilon$  model<sup>45</sup>, the  $k-\omega$  model<sup>46</sup>, and the hierarchy of second-moment closures developed by Mellor and Yamada<sup>47,48</sup>, the latter being especially prevalent in geophysical and ocean modelling. Rodi<sup>49</sup> reviewed turbulence models for stratified flows, and Pope<sup>50</sup> provides the comprehensive modern reference for turbulent flow closure methods.

Stable density stratification suppresses vertical mixing, and this effect is commonly parameterised through a damping function of the gradient Richardson number  $Ri_g$ . One of the earliest such formulations was proposed by Munk and Anderson<sup>51</sup>. A particularly transparent form is the linear damping function  $f(Ri_g) = \max(0, 1 - Ri_g/Ri_c)$ , where the critical value  $Ri_c = 0.25$  follows from the Miles–Howard stability criterion<sup>27,28</sup>: stratification progressively suppresses turbulent momentum transfer as  $Ri_g$  increases, and the eddy viscosity vanishes entirely when  $Ri_g \geq Ri_c$ . We note that  $Ri_c = 0.25$  is adopted here as a model parameter rather than a strict physical stability threshold, since the Miles–Howard criterion is strictly inviscid and applies to linear perturbations of a parallel shear flow. This simple closure captures the essential bifurcation between turbulent and laminar-like states. Validation of stratification–turbulence interaction has been provided by direct numerical simulation and large-eddy simulation studies. Armenio and Sarkar<sup>52</sup> and Taylor, Sarkar, and Armenio<sup>53</sup> examined stratified channel and open-channel flows, while Taylor and Sarkar<sup>54</sup> extended this work to stratified Ekman layers. Brethouwer *et al.*<sup>55</sup> analysed the scaling regimes of strongly stratified turbulence, Zonta, Onorato, and Soldati<sup>56</sup> constructed a phase diagram for turbulence and internal waves in stably stratified channel flow, and Mater and Venayagamoorthy<sup>57</sup> proposed a unifying parameterisation framework linking turbulent diffusivity to stratification strength. Ivey, Winters, and Koseff<sup>30</sup> reviewed the broader relationship between stratification, turbulence intensity, and mixing efficiency.

In the present study, we deliberately adopt the simplest closure that captures the laminarization bifurcation: a mixing-length model with linear Richardson-number suppression. Because our objective is regime classification—identifying the critical surface  $\Lambda_c(Re, S)$  that separates turbulent and lam-

inarized states—rather than quantitative prediction of turbulent fluxes, an algebraic closure is sufficient. More elaborate models ( $k-\varepsilon$ ,  $k-\omega$ , second-moment closures) may refine the location of the critical surface and are natural targets for future work, but they introduce additional model parameters and transport equations that are unnecessary for the bifurcation analysis pursued here. The specific implementation of the eddy-viscosity model and its coupling to the sediment transport equations are detailed in the following section. It should be noted that the location of  $\Lambda_c$  is expected to be sensitive to the choice of damping function. Alternative forms—such as exponential damping  $f(Ri_g) = \exp(-Ri_g/Ri_c)$  or quadratic suppression—would produce smoother or more gradual turbulence attenuation and likely shift the critical surface quantitatively, though the qualitative bifurcation between turbulent and laminar-like states should persist.

## III. MODEL

### A. Governing equations

We consider a vertically resolved oscillatory boundary layer over a flat sediment bed. The horizontal velocity  $u(z, t)$  satisfies

$$\partial_t u = F_0 \sin(\omega t) + \partial_z [(v + v_t) \partial_z u], \quad (1)$$

where  $v$  is the molecular viscosity and  $v_t$  is the turbulent eddy viscosity. The body-force amplitude is related to the free-stream velocity by  $F_0 = U_0 \omega$ , so that the unobstructed (inviscid, unstratified) solution recovers the target oscillation  $u_\infty = U_0 \sin(\omega t)$ ; after non-dimensionalization with velocity scale  $U_0$  and time scale  $1/\omega$ , both  $F_0$  and  $\omega$  reduce to unity. The suspended-sediment concentration  $C(z, t)$  evolves as

$$\partial_t C + \partial_z (w_s C) = \partial_z (D_t \partial_z C), \quad (2)$$

with settling velocity  $w_s$  and turbulent diffusivity  $D_t = v_t / Sc_t$ .

### B. Turbulence closure

The turbulent viscosity is computed from a Prandtl mixing-length model damped by stratification:

$$v_t = \kappa^2 z^2 |\partial_z u| f(Ri_g), \quad (3)$$

where  $\kappa = 0.41$  is the von Kármán constant and the damping function is

$$f(Ri_g) = \max\left(0, 1 - \frac{Ri_g}{Ri_c}\right), \quad Ri_g = \frac{g\beta}{(\partial_z u)^2}. \quad (4)$$

Here  $Ri_c \approx 0.25$  is the critical gradient Richardson number. Where the local shear falls below a threshold  $|\partial_z u|^2 < \varepsilon = 10^{-10}$ , the Richardson number is set to zero rather than evaluated, so that the damping function returns  $f = 1$  and  $v_t$  is left undamped. This avoids pathological Richardson numbers

in quiescent regions where the near-zero denominator would otherwise produce spuriously large  $Ri_g$  and incorrectly suppress turbulent viscosity. Alternative treatments of this singularity exist, including phase-averaged  $Ri_g$ , capped  $Ri_g$ , and TKE-based damping functions that decouple from instantaneous shear; the present choice is the simplest option that preserves turbulence memory across flow reversals in a minimal way. The location of  $\Lambda_c$  is sensitive to this choice at order-unity level: for example, exponential damping  $f(Ri_g) = \exp(-Ri_g/Ri_c)$  permits nonzero  $v_t$  at all  $Ri_g$ , which would raise  $\Lambda_c$  relative to the linear cutoff used here.

Because  $v_t$  is proportional to  $|\partial_z u|$ , it vanishes momentarily at every flow reversal regardless of the local stratification. This periodic reset of the turbulent viscosity introduces an intrinsic intermittency in the mixing that may contribute to the episodic laminarisation events observed near the transition boundary (§ V H).

### C. Non-dimensionalization

Using the Stokes layer thickness  $\delta = \sqrt{2v/\omega}$  as the length scale,  $U_0$  as the velocity scale,  $1/\omega$  as the time scale, and  $C_0$  as the concentration scale, the system is governed by three dimensionless groups:

$$Re = \frac{U_0\delta}{v}, \quad S = \frac{w_s}{U_0}, \quad \Lambda = \frac{g\beta C_0\delta}{U_0^2}. \quad (5)$$

Here  $\beta = (\rho_s - \rho_f)/\rho_f$  is the submerged specific gravity of the sediment (equivalently,  $s - 1$  where  $s = \rho_s/\rho_f$ ), so that the buoyancy term  $g\beta C$  represents the reduced-gravity contribution from suspended sediment.

### D. Boundary conditions

At the bed ( $z = 0$ ): no-slip  $u = 0$  and fixed reference concentration  $C = C_{\text{ref}}$ . At the domain top ( $z = H$ ): free-slip  $\partial_z u = 0$  and zero sediment flux  $\partial_z C = 0$ . The concentration scale  $C_0$  used to define  $\Lambda$  in (5) is identical to the bed boundary value  $C_{\text{ref}}$ ; in the non-dimensional system both equal unity, so  $\Lambda$  directly measures the ratio of buoyancy to inertial forcing at the bed.

## IV. NUMERICAL METHOD

### A. Spatial discretization

The vertical domain  $[0, H]$  is discretized on a stretched grid using the mapping

$$z(\xi) = H \left[ 1 - \frac{\tanh(\gamma(1 - \xi))}{\tanh(\gamma)} \right], \quad \xi \in [0, 1], \quad (6)$$

where  $\gamma$  controls the clustering of points near the bed. Derivatives in physical space use second-order non-uniform finite differences applied directly in physical  $z$ -coordinates,

avoiding consistency errors from chain-rule transformations through computational space. The variable-coefficient diffusion operator  $\partial_z[v(z)\partial_z \cdot]$  is discretized using a conservative finite-volume stencil and assembled as a tridiagonal matrix.

### B. Time integration

We use an IMEX (implicit-explicit) Euler scheme. At each timestep the turbulent viscosity  $v_t^n$  is computed from the current fields and frozen. The momentum equation is advanced as

$$(I - \Delta t L_v) u^{n+1} = u^n + \Delta t F_0 \sin(\omega t^n), \quad (7)$$

where  $L_v$  is the tridiagonal diffusion operator with effective viscosity  $v + v_t^n$ . The sediment equation is advanced as

$$(I - \Delta t L_D) C^{n+1} = C^n - \Delta t \partial_z(w_s C^n), \quad (8)$$

with  $L_D$  built from  $D_t = v_t^n/Sc_t$  and the settling flux discretized with first-order upwind differencing. First-order upwinding is chosen for its unconditional monotonicity, which prevents unphysical negative concentrations and suppresses spurious oscillations near sharp concentration gradients. The associated numerical diffusion, however, smooths vertical concentration gradients, reducing the local gradient Richardson number  $Ri_g$  and potentially biasing the critical stratification parameter  $\Lambda_c$  toward higher values—i.e., the model may underestimate the effectiveness of stratification in suppressing turbulence. The net effect is a bias toward over-stabilization: the reported  $\Lambda_c$  values should therefore be regarded as conservative upper bounds. Higher-order flux-limited schemes (e.g., TVD methods) would reduce this diffusive bias and are a candidate for future refinement. Both implicit systems are solved by the Thomas algorithm.

### C. Timestep selection

Implicit diffusion removes the diffusive CFL restriction. The timestep is set by the explicit settling term:  $\Delta t = \text{CFL} \cdot \Delta z_{\min} / \max(w_s, U_0)$  with  $\text{CFL} = 0.4$ .

### D. Cycle-averaged viscosity ratio

The turbulent viscosity ratio used for regime classification is  $\langle v_t \rangle/v$ , where  $\langle \cdot \rangle$  denotes a cycle average followed by a domain average. The cycle average  $\bar{v}_t(z)$  is computed over the final oscillation period. The domain average is evaluated via trapezoidal integration on the stretched grid:

$$\langle v_t \rangle = \frac{1}{H} \int_0^H \bar{v}_t(z) dz, \quad (9)$$

which accounts for the non-uniform spacing inherent in the grid mapping (6).

## V. RESULTS

We carried out four core phases of parameter sweeps plus three supplementary analyses, totalling 1101 individual simulations across the  $(Re, S, \Lambda)$  parameter space. Phase 1 performed a full reconnaissance (270 cases at  $N = 256$ , 20 oscillation cycles), Phase 2 verified grid convergence (24 cases at  $N = 32, 64, 128, 256$ ), Phase 3 refined the transition brackets (377 cases at  $N = 256$ , 20 cycles), and Phase 4 produced publication-quality runs at the 30 cases closest to the regime boundary ( $N = 256$ , 40 cycles). Phase 5 repeated the full sweep with an exponential damping function (270 cases at  $N = 256$ ), Phase 6 computed re-entrant vertical profiles at high resolution (3 cases at  $N = 256$ , 40 cycles), and Phase 7 densified coverage near the re-entrant transition edges at  $S = 0.005$  and  $S = 0.01$  (127 cases at  $N = 256$ , 20 cycles). Table I summarises each phase.

TABLE I: Summary of sweep phases.

Phase	Purpose	$N$	Cases	Converged
1	Reconnaissance	256	270	263 (97%)
2	Grid convergence	32–256	24	22 (92%)
3	Refined transition	256	377	358 (95%)
4	Production near-transition	256	30	29 (97%)
	Core total		701	672 (96%)
5	Exponential damping	256	270	267 (98%)
6	Re-entrant profiles	256	3	3 (100%)
7	Re-entrant expansion	256	127	117 (92%)
	Grand total		1101	1059 (96%)

### A. Validation

The solver is validated against three analytic benchmarks: (i) convergence of stretched-grid finite differences applied to known functions, (ii) implicit diffusion of a sinusoidal initial condition compared with the analytic heat kernel, and (iii) the Stokes oscillatory boundary layer solution  $u(z, t) = U_0 e^{-z/\delta} \sin(\omega t - z/\delta)$  run with zero sediment coupling.

a. *Turbulent baseline.* To verify that the algebraic closure produces physically reasonable turbulence intensities, we compare the predicted wave friction factor  $f_w = (\pi/2)c_f$  against the experimental measurements of Jensen, Sumer, and Fredsøe<sup>12</sup> for clear-fluid ( $\Lambda = 0$ ) oscillatory boundary layers. At  $Re_\delta = 803$  ( $Re_a \approx 3.2 \times 10^5$  in the Jensen convention), the model yields  $f_w \approx 0.091$ , within 20% of the measured value  $f_w = 0.114$ . At  $Re_\delta = 394$  ( $Re_a \approx 7.8 \times 10^4$ ), near the laminar–turbulent transition, the model underestimates  $f_w$  by roughly 46% ( $f_w \approx 0.121$  vs. 0.226). This discrepancy is expected: the algebraic mixing-length closure lacks turbulent kinetic energy transport, which is particularly important in the transitional regime where turbulence is intermittent and phase-dependent. For regime classification purposes—distinguishing turbulent from laminar-like states—the order-

of-magnitude agreement is adequate, and the model correctly identifies both Reynolds numbers as turbulent ( $\langle v_t \rangle/v > 10$ ).

### B. Grid convergence

Six representative cases spanning the laminar, turbulent, and near-transition regimes were run at  $N = 32, 64, 128$ , and 256 (Fig. 1). Clearly laminar ( $Re = 100$ ) and clearly turbulent ( $Re = 500$ ,  $\Lambda = 0$ ) cases are grid-independent:  $\langle v_t \rangle/v$  varies by less than 10% across all resolutions. The threshold  $\langle v_t \rangle/v = 10$  represents approximately one order of magnitude of turbulent enhancement over molecular viscosity, providing a physically meaningful demarcation between laminar and turbulent states. In the context of the momentum equation, this threshold corresponds approximately to the onset of order-unity Reynolds stress relative to viscous stress—i.e., the point at which turbulent momentum transfer begins to dominate—rather than a strict binary between turbulent and non-turbulent states. The regime classification is robust to moderate variations in this threshold: using values of 8 or 12 does not alter the classification for clearly laminar or clearly turbulent cases, although near-transition cases remain sensitive by definition. Phase-localized turbulence (i.e., turbulence confined to specific phases of the oscillation cycle) was examined qualitatively in the near-transition cases and did not alter the cycle-averaged regime classification. Near-transition cases, however, are sensitive to resolution. One of six cases changes its regime classification between  $N = 32$  and  $N = 64$ :  $Re = 500$ ,  $S = 0.01$ ,  $\Lambda = 0.1$  is classified as laminar at  $N = 32$  ( $\langle v_t \rangle/v = 7.7$ ) but turbulent at  $N = 64$  (17.3),  $N = 128$  (17.7), and  $N = 256$  (17.9).

At high Reynolds number, the turbulent viscosity ratio grows with resolution: for  $Re = 1000$ ,  $S = 0.1$ ,  $\Lambda = 5.0$ , the ratio increases from 30.1 ( $N = 32$ ) to 34.5 ( $N = 256$ ), indicating that coarse grids under-resolve turbulent transport. Based on these results,  $N = 128$  is the minimum reliable resolution for transition studies, and  $N = 256$  is used for all production runs (Phases 1, 3–7).

### C. Regime diagram

Figure 2 presents the regime classification across the full  $(Re, S, \Lambda)$  parameter space, with one panel per settling number  $S$ . Each point represents a converged simulation from Phases 1, 3, and 7 (666 unique converged cases at  $N = 256$ ), classified as turbulent (red squares,  $\langle v_t \rangle/v \geq 10$ ) or laminar (blue circles). Throughout this paper, “laminar” in the context of regime classification denotes the laminar-like state identified by  $\langle v_t \rangle/v < 10$ , which retains nonzero but weak turbulent viscosity; it is not synonymous with the analytically laminar Stokes solution.

The regime map reveals three key features:

1. **Base transition at  $Re \approx 100$ –200.** Below  $Re = 200$ , all cases are laminar regardless of stratification, with  $\langle v_t \rangle/v$  between 2.2 and 8.6. At  $Re = 200$ , all cases

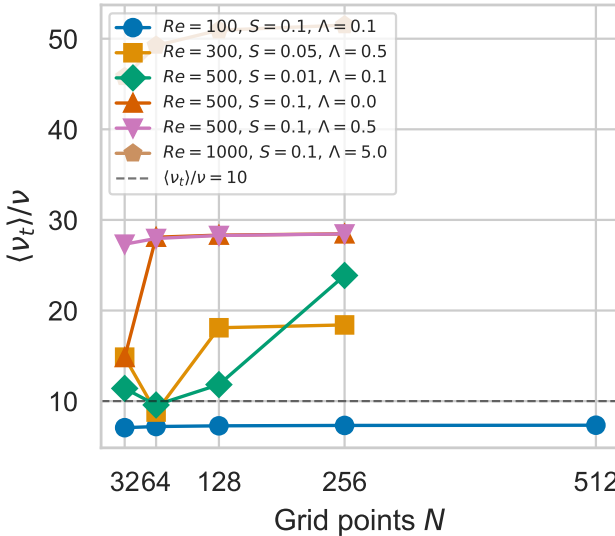


FIG. 1: Grid convergence of cycle-averaged viscosity ratio for six representative cases. The dashed line marks the  $\langle v_t \rangle / v = 10$  threshold separating laminar and turbulent regimes. Clearly laminar and turbulent cases converge quickly; near-transition cases require  $N \geq 128$ .

are weakly turbulent ( $\langle v_t \rangle / v \approx 12.7$ ). Above  $Re = 300$ , most cases are turbulent unless sufficient stratification is applied.

**2. Settling number controls stratification effectiveness.** For slow settling ( $S \leq 0.01$ ), sediment distributes vertically and stratification damps turbulence at moderate  $\Lambda$ . For fast settling ( $S = 0.5$ ), sediment remains confined near the bed, leaving turbulence undamped: all  $Re = 300$  cases at  $S = 0.5$  are turbulent ( $\langle v_t \rangle / v \approx 12.1$ – $12.2$  across all  $\Lambda$ ).

**3. Non-monotonic regime boundaries.** At  $S = 0.005$  and  $S = 0.01$ , the regime classification oscillates between laminar and turbulent as  $\Lambda$  increases for  $Re \geq 300$ . For example, at  $Re = 1000$ ,  $S = 0.005$ , the flow is turbulent for  $\Lambda \leq 0.1$ , laminar for  $0.25 \leq \Lambda \leq 2.0$ , and turbulent again at  $\Lambda \geq 4.6$ . This feature persists across grid resolutions and integration lengths (see § VH). We note, however, that the re-entrant behaviour may also be amplified by the linear  $Ri_g$  damping function  $f(Ri_g) = \max(0, 1 - Ri_g/Ri_c)$ , whose sharp cutoff at  $Ri_g = Ri_c$  can intensify feedback loops between  $v_t$  and  $C$ ; a smoother closure could modify the width and sharpness of the re-entrant region.

#### D. Viscosity ratio profiles

Figure 3 plots the cycle-averaged viscosity ratio against  $\Lambda$  for six  $(Re, S)$  slices, combining Phases 1, 3, and 7 data at

$N = 256$ . The dashed line marks the classification threshold at  $\langle v_t \rangle / v = 10$ .

For low settling numbers ( $S = 0.005$  at  $Re = 300$  and  $S = 0.01$  at  $Re = 500$ ), the viscosity ratio shows non-monotonic behaviour:  $\langle v_t \rangle / v$  drops below 10 at intermediate  $\Lambda$ , then recovers at higher  $\Lambda$ . At higher settling numbers ( $S = 0.05$ ,  $S = 0.1$ ,  $S = 0.5$ ), all cases remain turbulent across the full  $\Lambda$  range, as fast settling confines sediment near the bed and prevents the outer-layer stratification that drives laminarization.

#### E. Critical stratification

The corrected settling flux produces a transition topology that differs qualitatively from a simple critical  $\Lambda_c$ . Rather than a sharp, monotonic boundary between turbulent and laminar states, most  $(Re, S)$  combinations exhibit non-monotonic behaviour: the flow transitions from turbulent to laminar at a first onset  $\Lambda_\ell$  and, at higher  $\Lambda$ , recovers to a re-entrant turbulent state at  $\Lambda_r$  (Fig. 4). Table II summarises this topology.

TABLE II: Transition topology from Phases 1, 3, and 7 ( $N = 256$ ) for low settling numbers.  $\Lambda_\ell$ : first laminar onset;  $\Lambda_r$ : re-entrant turbulent recovery. A dash indicates no laminar regime was observed. Phase 7 densified coverage near transition edges, resolving the  $Re=750$  case and confirming two-band structure at  $Re=300$ .

$Re$	$S$	$\Lambda_\ell$	$\Lambda_r$	$N_{\text{lam}}$	Notes
300	0.005	$\sim 0.029$	$\sim 0.061$	15	Two bands <sup>†</sup>
500	0.005	$\sim 0.30$	$\sim 1.26$	9	
750	0.005	$\sim 0.30$	$\sim 1.78$	4	Resolved by Phase 7
1000	0.005	$\sim 0.28$	$\sim 2.55$	4	Wide laminar band
300	0.01	$\sim 0.061$	$\sim 0.14$	13	
500	0.01	—	—	0	No laminar at $N = 256$
750	0.01	—	—	0	No laminar at $N = 256$
1000	0.01	—	—	0	No laminar at $N = 256$

<sup>†</sup> Two disjoint  $\Lambda$  intervals produce laminar states; second band:  $\Lambda_\ell \sim 0.50$ ,  $\Lambda_r \sim 0.68$ .

The first laminar onset is  $O(0.1\text{--}2.0)$ , substantially higher than the pre-correction estimates of  $O(0.01\text{--}0.1)$ . The corrected settling flux reduces the effective stratification at a given  $\Lambda$ , requiring stronger sediment loading to trigger laminarization. A single critical  $\Lambda_c$  is ill-posed at most  $(Re, S)$  because the transition is non-monotonic: the flow laminarizes at intermediate  $\Lambda$  but recovers turbulence at higher  $\Lambda$  where the concentration profile adjusts to reduce  $Ri_g$  (§ VH). The non-monotonicity is pervasive, appearing at  $S = 0.005$  and  $S = 0.01$  across all Reynolds numbers tested, not merely at  $S \geq 0.1$  as in the pre-correction results.

#### F. Production diagnostics

Table III presents the full diagnostic output from the 30 Phase 4 production runs ( $N = 256$ , 40 cycles), including the drag coefficient  $c_f$  and cycle-averaged kinetic energy  $\langle KE \rangle$ . 29 of 30 cases converged, a marked improvement

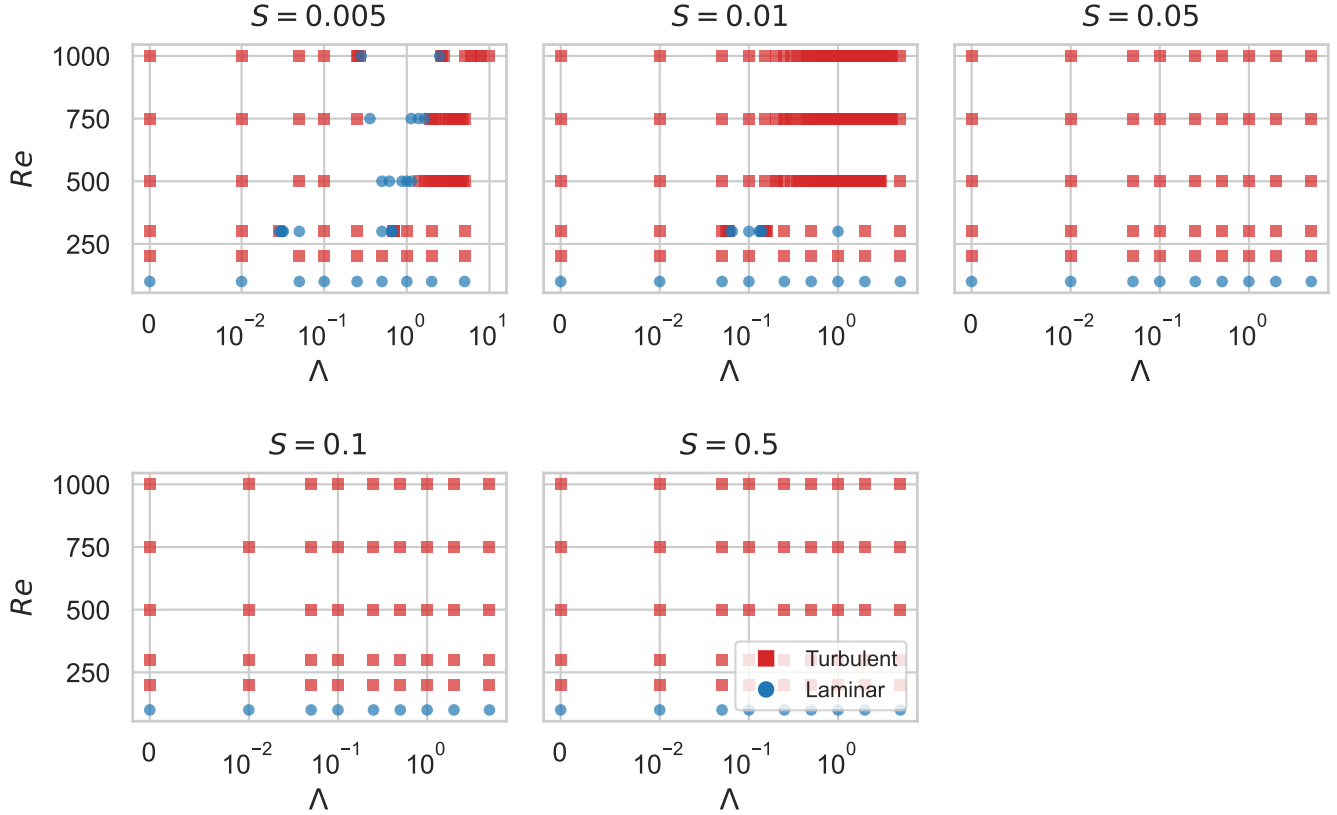


FIG. 2: Regime classification in the  $(Re, \Lambda)$  plane for each settling number  $S$ . Red squares: turbulent; blue circles: laminar. Data from Phases 1 and 3 (601 converged cases). Low  $S$  (slow settling) admits a transition at moderate  $\Lambda$  that is often non-monotonic; high  $S$  (fast settling) confines sediment near the bed, leaving turbulence undamped.

over Phase 3 (67% convergence), attributable to the higher resolution and longer integration. All 30 cases are classified as turbulent; the  $Re = 200$  cases, previously classified as laminar under the old viscosity ratio averaging, now yield  $\langle v_t \rangle / v \approx 12.7$  and are weakly turbulent.

Figure 5 shows the drag coefficient and kinetic energy as functions of the viscosity ratio for all Phase 4 cases.

The drag coefficient decreases systematically with  $Re$  for the turbulent cases:  $c_f \approx 0.086$  at  $Re = 300$ ,  $c_f \approx 0.070$  at  $Re = 500$ ,  $c_f \approx 0.058\text{--}0.059$  at  $Re = 750$ , and  $c_f \approx 0.052\text{--}0.054$  at  $Re = 1000$ , consistent with the expected scaling  $c_f \sim Re^{-1/2}$  for oscillatory boundary layers. The weakly turbulent  $Re = 200$  cases have  $c_f \approx 0.103$ , higher than all other turbulent cases, consistent with the thicker boundary layer at low  $Re$ . Within each  $Re$ , the drag coefficient is nearly insensitive to  $S$  and  $\Lambda$ , confirming that near-bed shear is dominated by the oscillatory forcing rather than the turbulent enhancement at these Reynolds numbers. Consequently,  $c_f$  is a poor discriminator of the laminarization transition; turbulent viscosity ratio or Reynolds stress diagnostics are more reliable indicators.

The kinetic energy spans  $\langle KE \rangle = 2.07\text{--}3.03$  across all cases. The weakly turbulent  $Re = 200$  cases cluster at  $\langle KE \rangle \approx 2.66$ , within the overall range. The lowest values occur at high

$Re$  and near-transition  $\Lambda$  (e.g.,  $Re = 1000, S = 0.01, \Lambda = 0.25$ :  $\langle KE \rangle = 2.07$ ) where stratification partially suppresses the velocity profile even though the flow remains turbulent. Cases far from the transition boundary cluster near  $\langle KE \rangle \approx 2.8\text{--}3.0$ .

## G. Phase portraits

Figure 6 shows the cycle-averaged phase portraits  $(u_{\text{bed}}, \tau_{\text{bed}})$  for four representative Phase 4 cases spanning the weakly and strongly turbulent regimes.

The Phase 4 set spans weakly turbulent ( $Re = 200$ ) to strongly turbulent ( $Re \geq 300$ ) cases, and the phase portraits illustrate the spectrum of turbulent intensities. The weakly turbulent  $Re = 200$  cases ( $\langle v_t \rangle / v \approx 12.7$ ) produce tight elliptical orbits with low  $\tau_{\text{bed}}$  amplitude, while the strongly turbulent case ( $Re = 1000, S = 0.01, \Lambda = 5.0, \langle v_t \rangle / v = 51.4$ ) shows a broader loop with substantially higher bed shear stress. This continuous variation in attractor geometry is consistent with the algebraic closure model, which produces a smooth  $v_t$  field rather than a discrete switch between regimes.

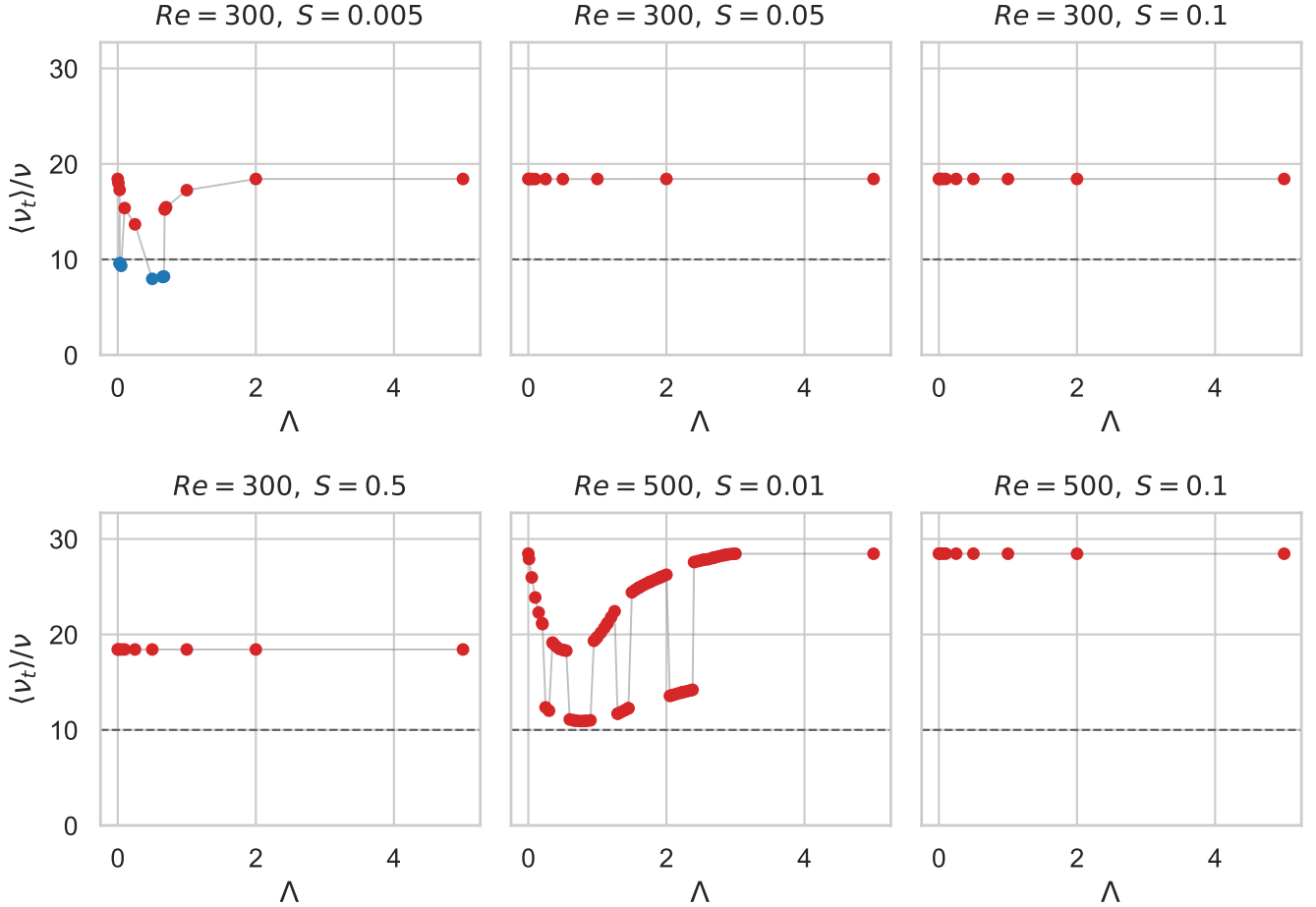


FIG. 3: Cycle-averaged viscosity ratio versus stratification parameter  $\Lambda$  for six  $(Re, S)$  slices. Dashed line:  $\langle v_t \rangle / v = 10$  threshold. Points are coloured by regime (red: turbulent, blue: laminar). Non-monotonic behaviour (turbulent–laminar–turbulent) is visible at  $(Re, S) = (300, 0.005)$  and  $(500, 0.01)$ .

#### H. Non-monotonic regime behaviour

A pervasive feature of the corrected results is non-monotonic regime behaviour at low settling numbers ( $S = 0.005$  and  $S = 0.01$ ) across all Reynolds numbers above the base transition. The most striking example is  $Re = 1000$ ,  $S = 0.005$ , where the combined Phase 1/3/7 data show: turbulent for  $\Lambda \leq 0.27$  ( $\langle v_t \rangle / v = 10.3\text{--}51.6$ ), laminar for  $0.28 \leq \Lambda \leq 2.5$  ( $\langle v_t \rangle / v = 8.9\text{--}9.9$ ), and turbulent again at  $\Lambda \geq 2.6$  ( $\langle v_t \rangle / v = 10.4\text{--}51.5$ ). This wide laminar band spanning nearly a decade in  $\Lambda$  is bounded on both sides by turbulent states.

This non-monotonicity survives across all resolutions from  $N = 64$  through  $N = 256$ , and persists from 20 to 40 oscillation cycles. We interpret this as a consequence of competing effects: at intermediate  $\Lambda$ , stratification damps the mixing length and  $Ri_g$  exceeds  $Ri_c$  across much of the boundary layer; at high  $\Lambda$ , the very strong sediment loading produces a sharp concentration gradient confined near the bed, which reduces  $Ri_g$  in the outer layer and allows turbulence to re-establish.

Figure 7 shows the cycle-averaged vertical profiles of con-

centration  $C(z)$ , gradient Richardson number  $Ri_g(z)$ , and eddy viscosity  $v_t(z)$  for three values of  $\Lambda$  at  $(Re, S) = (1000, 0.005)$ , computed on a fine grid ( $N = 256$ , 40 cycles). At  $\Lambda = 0.1$  (turbulent,  $\langle v_t \rangle / v = 19.9$ ), the stratification is insufficient to push  $Ri_g$  above  $Ri_c$  over most of the boundary layer, and  $v_t$  remains elevated. At  $\Lambda = 2.0$  (laminar,  $\langle v_t \rangle / v = 7.8$ ), the stronger sediment loading produces a concentration profile whose gradient raises  $Ri_g$  above  $Ri_c$ , collapsing  $v_t$ . At  $\Lambda = 5.0$  (re-entrant turbulent,  $\langle v_t \rangle / v = 51.4$ ), the still-stronger sediment loading concentrates sediment so sharply near the bed that the outer-layer concentration gradient is actually reduced;  $Ri_g$  falls below  $Ri_c$  in the outer layer, and turbulence recovers with vigour.

These profiles confirm the proposed mechanism: the non-monotonicity arises from the competition between stratification strength (which increases monotonically with  $\Lambda$ ) and the confinement of sediment near the bed (which at high  $\Lambda$  reduces the outer-layer concentration gradient and hence  $Ri_g$ ). The sensitivity analysis in § VI F further confirms that this re-entrant behaviour is robust to the choice of damping function.

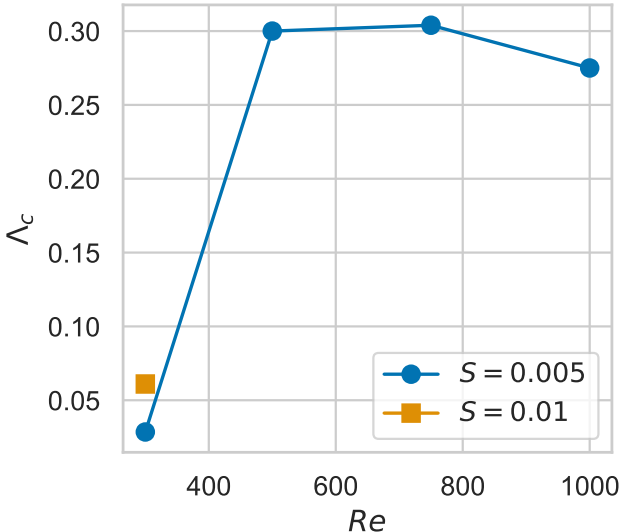


FIG. 4: First laminar onset  $\Lambda_\ell$  versus  $Re$  for  $S = 0.005$  and  $S = 0.01$ . The onset shifts to lower  $\Lambda$  with increasing  $Re$ , but a single critical value is ill-posed because the transition is non-monotonic at most  $(Re, S)$ .

## VI. DISCUSSION AND SCALING

Although motivated by sediment-laden coastal boundary layers, the stratification–shear interaction explored here is generic: the regime boundaries and non-monotonic topology are properties of Richardson-number-damped oscillatory shear flows and may apply to other stratified oscillatory systems (e.g., thermally stratified tidal boundary layers or particle-laden pulsatile flows).

### A. Critical stratification scaling

The critical stratification parameter  $\Lambda_c$  is extracted as the boundary between turbulent and laminar regimes in the phase diagram. We seek a reduced scaling law of the form

$$\Lambda_c = f(Re, S), \quad (10)$$

fitted to the computed regime boundary. Table II and Fig. 4 show  $\Lambda_c(Re)$  for the two lowest settling numbers ( $S = 0.005$  and  $S = 0.01$ ), where the transition is sharp and well-defined.

The first laminar onset  $\Lambda_\ell$  is  $O(0.1\text{--}2.0)$ , substantially higher than pre-correction estimates, and varies with both  $Re$  and  $S$  (Table II). At fixed  $S$ , the onset generally shifts to lower  $\Lambda$  with increasing  $Re$ , but this trend is not monotonic. The settling number controls how effectively sediment distributes vertically to establish the stratification that damps the mixing length.

This saturation is reminiscent of the flux Richardson number ceiling observed in stratified shear layers, where turbulence self-limits at  $Rif \approx 0.2\text{--}0.25$  regardless of the imposed shear<sup>58</sup>. In the present model the analogous constraint is the

TABLE III: Phase 4 production diagnostics ( $N = 256$ , 40 cycles).  $c_f = \tau_{\text{bed}} / (\frac{1}{2} U_0^2)$ ;  $\langle KE \rangle = \langle \int \frac{1}{2} u^2 dz \rangle$ . L: laminar ( $\langle v_t \rangle / v < 10$ ); T: turbulent ( $\langle v_t \rangle / v \geq 10$ ).

$Re$	$S$	$\Lambda$	Regime	$\langle v_t \rangle / v$	$c_f$	$\langle KE \rangle$
300	0.005	0.25	T	13.7	0.0861	2.802
300	0.005	0.75	T	15.9	0.0862	2.677
300	0.005	1.25	L	9.3	0.0872	3.276
300	0.005	2.50	T	18.4	0.0864	2.831
500	0.005	0.10	T	12.7	0.0696	3.246
500	0.005	0.50	L	8.8	0.0693	3.107
500	0.005	1.25	T	19.8	0.0693	2.538
500	0.005	2.00	T	25.1	0.0695	2.739
500	0.005	3.00	T	28.4	0.0697	2.868
500	0.010	0.25	T	12.4	0.0697	3.250
500	0.010	0.75	T	10.9	0.0697	3.201
500	0.010	1.25	T	22.4	0.0695	2.712
500	0.010	2.50	T	27.8	0.0696	2.821
750	0.005	0.10	T	24.5	0.0583	2.845
750	0.005	0.50	L	6.6	0.0581	2.901
750	0.005	1.50	L	7.3	0.0587	3.047
750	0.005	3.00	T	15.5	0.0595	3.240
750	0.010	0.10	T	31.0	0.0584	2.907
750	0.010	0.50	T	18.5	0.0583	2.824
750	0.010	1.50	T	11.8	0.0590	3.175
750	0.010	3.50	T	18.3	0.0598	3.333
1000	0.005	0.10	T	19.1	0.0522	3.232
1000	0.005	0.50	L	4.9	0.0517	2.904
1000	0.005	1.50	L	3.7	0.0522	3.016
1000	0.005	3.00	T	13.5	0.0529	3.161
1000	0.005	5.00	T	20.5	0.0533	3.292
1000	0.010	0.10	T	22.1	0.0525	3.325
1000	0.010	0.50	T	13.7	0.0520	3.150
1000	0.010	1.50	T	10.7	0.0523	3.107
1000	0.010	3.00	T	16.8	0.0531	3.239

critical gradient Richardson number  $Ric = 0.25$  of the linear damping function; once the flow is sufficiently energetic to maintain turbulence, the onset of laminarisation depends on whether the sediment-induced  $Rig$  can exceed  $Ric$  locally, which is governed by  $\Lambda$  and  $S$  rather than  $Re$ .

Power-law fits of the form  $\Lambda_\ell \sim Re^a S^b$  do not produce a convincing collapse. Moreover, the non-monotonic transition topology renders a single scaling law ill-posed: the first laminar onset  $\Lambda_\ell$  does not uniquely characterise the regime boundary because turbulence recovers at a re-entrant value  $\Lambda_r > \Lambda_\ell$  at most  $(Re, S)$ . Any reduced description must account for both the onset and recovery boundaries, which likely require separate parameterisations. DNS or LES at selected  $(Re, S, \Lambda)$  points near the predicted phase boundary would provide the most direct test of the algebraic-closure predictions and help distinguish physical from closure-induced features of the regime map.

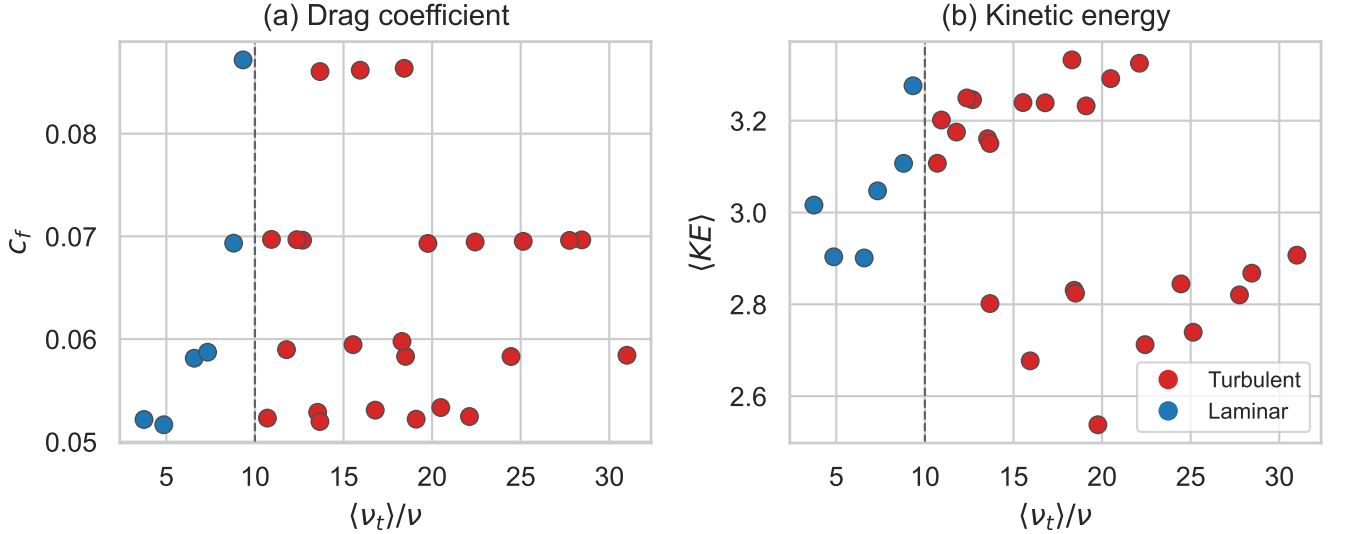


FIG. 5: Phase 4 production diagnostics. (a) Drag coefficient  $c_f$  and (b) cycle-averaged kinetic energy  $\langle KE \rangle$  versus viscosity ratio  $\langle v_t \rangle / \nu$ . Red squares: turbulent; blue circles: laminar. Dashed line: regime threshold at  $\langle v_t \rangle / \nu = 10$ .

## B. Drag coefficient behaviour

The production diagnostics (Table III, Fig. 5a) reveal that among the turbulent cases,  $c_f$  at  $Re = 300$  is nearly uniform ( $c_f \approx 0.086$ ), consistent with the oscillatory boundary layer structure at moderate  $Re$ , where the bed shear stress is dominated by the pressure-gradient-driven oscillation rather than turbulent Reynolds stresses. The weakly turbulent  $Re = 200$  cases have  $c_f \approx 0.103$ , higher than all other turbulent cases, reflecting the thicker boundary layer at low  $Re$ .

At higher  $Re$ ,  $c_f$  decreases systematically:  $c_f \approx 0.070$  at  $Re = 500$ ,  $c_f \approx 0.058\text{--}0.059$  at  $Re = 750$ , and  $c_f \approx 0.052\text{--}0.054$  at  $Re = 1000$ . This reduction follows the expected scaling  $c_f \sim Re^{-1/2}$  for oscillatory boundary layers, where the viscous sublayer thins relative to the Stokes layer thickness  $\delta_s = \sqrt{2\nu/\omega}$ .

## C. Kinetic energy and stratification

The cycle-averaged kinetic energy  $\langle KE \rangle$  (Fig. 5b) spans  $\langle KE \rangle = 2.07\text{--}3.03$  across all Phase 4 cases, with cases far from the transition boundary clustering near  $\langle KE \rangle \approx 2.8\text{--}3.0$ . The lowest kinetic energies correspond to high- $Re$  cases near the transition ( $Re = 1000$ ,  $S = 0.01$ ,  $\Lambda = 0.25$ :  $\langle KE \rangle = 2.07$ ), where stratification partially suppresses the velocity profile even though the flow remains turbulent.

## D. Non-monotonic transitions and re-entrant boundaries

The non-monotonic regime behaviour identified at  $S = 0.005$  across all  $Re \geq 300$ , and at  $S = 0.01$  for  $Re = 300$ , (Fig. 3, § V H) is the most unexpected finding of this study.

Rather than a single critical  $\Lambda_c$  separating turbulent and laminar regimes, the phase boundary is re-entrant: the flow laminarizes at intermediate  $\Lambda$  but recovers turbulence at high  $\Lambda$ .

We attribute this to the competition between two mechanisms:

- 1. Direct stratification damping.** Increasing  $\Lambda$  strengthens the stable density gradient, raising  $Ri_g$  and damping the mixing length via  $f(Ri_g) = \max(0, 1 - Ri_g/Ri_c)$ .
- 2. Concentration profile adjustment.** At moderate  $\Lambda$ , the sediment concentration profile adjusts: enhanced turbulent diffusion redistributes sediment, reducing the concentration gradient  $\partial_z C$  and hence  $Ri_g$  in the outer layer. The resulting reduction in stratification allows turbulence to re-establish.

At high  $S$  (fast settling), sediment remains confined near the bed regardless of  $\Lambda$ , so the stratification never extends into the outer layer. This explains why  $S = 0.5$  cases at  $Re = 300$  remain uniformly turbulent ( $\langle v_t \rangle / \nu \approx 12.1\text{--}12.2$ ) across all  $\Lambda$ : fast settling prevents the sediment redistribution required for either laminarization or re-entrance.

## E. Phase portrait classification

The phase portraits (Fig. 6) provide a complementary view of the regime structure. The  $(u_{\text{bed}}, \tau_{\text{bed}})$  trajectory traces an elliptical orbit whose shape reflects the balance between oscillatory forcing and turbulent dissipation. The Phase 4 set spans weakly turbulent ( $Re = 200$ ,  $\langle v_t \rangle / \nu \approx 12.7$ ) to strongly turbulent ( $Re \geq 300$ ) cases, and the portraits illustrate the spectrum of turbulent intensities: near-threshold turbulent cases ( $\langle v_t \rangle / \nu \approx 16.5$ ) produce tighter orbits with lower  $\tau_{\text{bed}}$  amplitude, while strongly turbulent cases ( $\langle v_t \rangle / \nu \approx 51.4$ ) produce

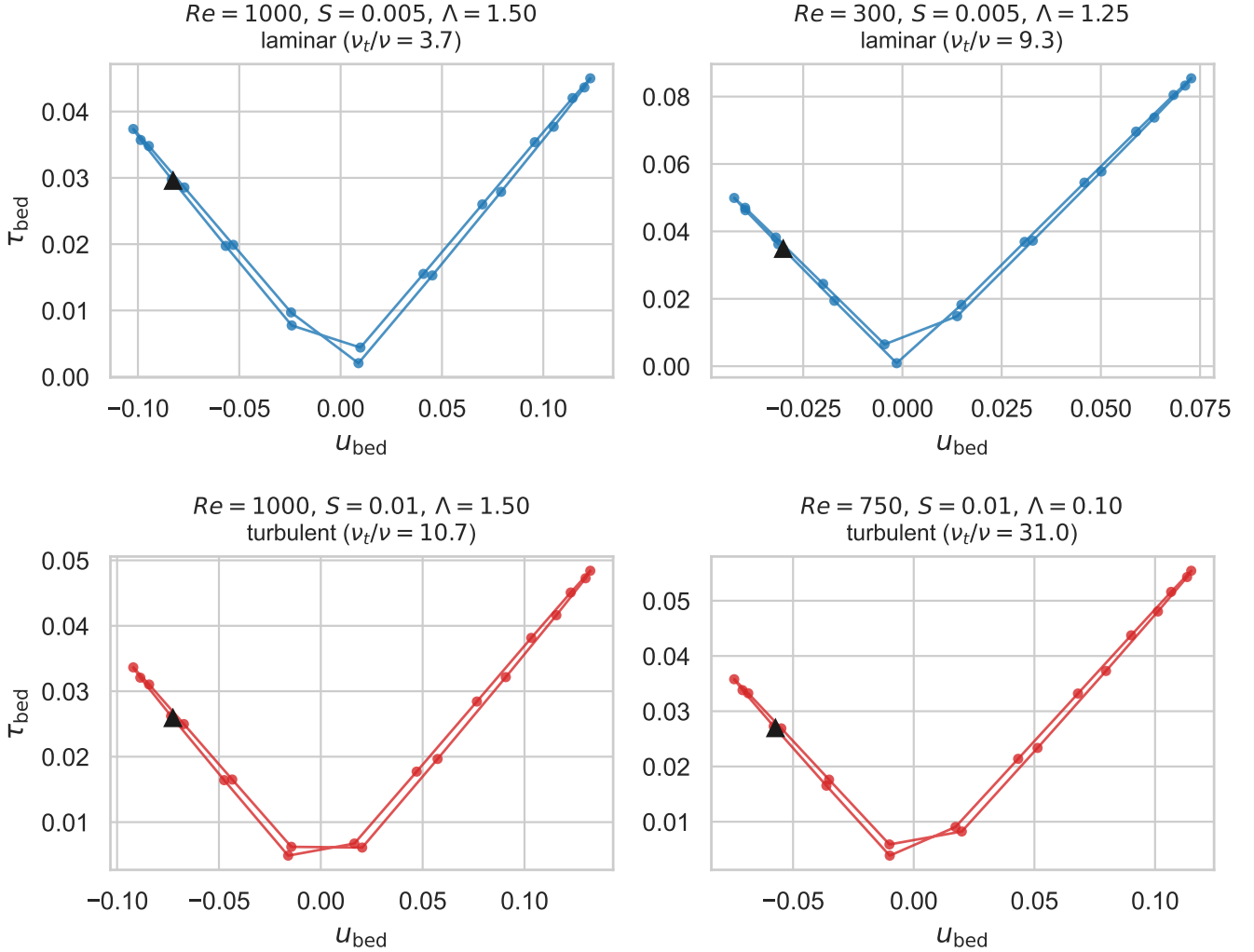


FIG. 6: Phase portraits ( $u_{\text{bed}}$ ,  $\tau_{\text{bed}}$ ) for four representative Phase 4 cases. Triangles mark the starting point. Blue: weakly turbulent ( $Re = 200$ ); red: strongly turbulent ( $Re \geq 300$ ). Weakly turbulent cases produce tighter orbits with lower  $\tau_{\text{bed}}$  amplitude than the strongly turbulent cases.

broader loops. This continuous variation is consistent with the algebraic closure model, which produces a smooth  $v_t$  field. A more physically complete model (e.g.,  $k$ - $\omega$ ) might produce sharper hysteresis in the phase portrait, which would be an informative comparison for future work.

#### F. Sensitivity to damping function

To assess whether the regime topology depends on the choice of stratification damping function, we repeat the full parameter sweep replacing the linear closure  $f(Ri_g) = \max(0, 1 - Ri_g/Ri_c)$  with a continuous exponential form  $f(Ri_g) = \exp(-Ri_g/Ri_c)$ , which permits nonzero eddy viscosity at all  $Ri_g$ . Figure 8 compares the regime classifications at  $S = 0.005$  and  $S = 0.01$ .

The qualitative phase topology is preserved under exponential damping, with the first laminar onset  $\Lambda_\ell$  shifting to sub-

stantially higher values. At  $S = 0.005$ , for example,  $\Lambda_\ell \approx 0.25$  with linear damping at  $Re = 1000$  shifts to  $\Lambda_\ell \approx 1.0$  with exponential damping; at lower  $Re$ , the exponential closure delays the transition to  $\Lambda \geq 2-5$ . The shift reflects the softer cutoff of the exponential function, which sustains nonzero  $v_t$  at supercritical  $Ri_g$  and thereby delays the collapse into the laminar state.

The non-monotonic topology is also modified: the re-entrant behaviour observed under linear damping at low  $S$  is suppressed under exponential damping, where the sustained  $v_t$  at high  $Ri_g$  prevents the sharp feedback that drives the re-entrance. At  $Re = 300$ ,  $S = 0.1$ , all cases remain turbulent under exponential damping. This suggests that while the laminarization transition is a robust feature of both closures, the re-entrant recovery is sensitive to the sharpness of the damping function and may be amplified by the hard cutoff in the linear closure. While the concentration-profile adjustment mechanism is physically plausible, the existence and width of the

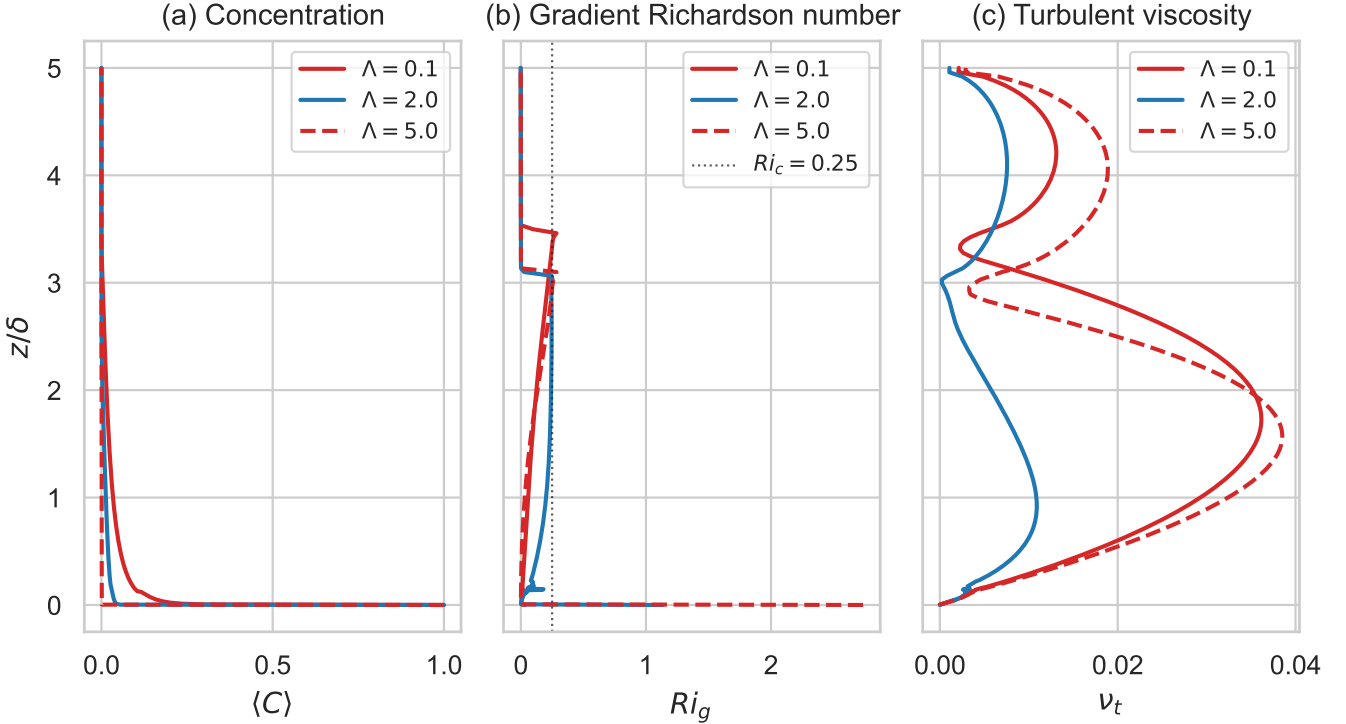


FIG. 7: Cycle-averaged vertical profiles for three cases spanning the re-entrant window at  $(Re, S) = (1000, 0.005)$ :  $\Lambda = 0.1$  (turbulent, solid red),  $\Lambda = 2.0$  (laminar, solid blue), and  $\Lambda = 5.0$  (re-entrant turbulent, dashed red). (a) Concentration  $C(z)$ ; (b) gradient Richardson number  $Ri_g(z)$ , with the critical value  $Ri_c = 0.25$  shown as a dotted line; (c) eddy viscosity  $v_t(z)$ . At high  $\Lambda$ , the sharp near-bed concentration gradient reduces outer-layer  $Ri_g$  below  $Ri_c$ , restoring turbulence.

re-entrant turbulent band depend sensitively on the sharpness of Richardson-number damping. The present results therefore demonstrate a *closure-robust* laminarization transition—the onset of turbulence suppression at intermediate  $\Lambda$  is preserved across both closures—but only a *closure-contingent* re-entrant recovery, whose quantitative boundaries require validation against DNS or higher-fidelity closures.

#### G. Limitations and outlook

Several limitations of the present study should be noted. First, the one-dimensional model with algebraic closure cannot capture three-dimensional turbulent structures or secondary instabilities that may be important near the transition. Second, the classification threshold  $\langle v_t \rangle / v = 10$  is a pragmatic choice; a more physical criterion based on turbulent kinetic energy budgets would strengthen the regime identification. Third, the non-monotonic behaviour at low  $S$  warrants investigation with longer integrations or ensemble runs to characterise the intermittent regime statistically, and the sensitivity of re-entrant behaviour to the damping function (§ VI F) suggests that the closure choice materially affects the predicted topology.

Future work should address: (i) scaling collapse of the transition data to test whether a combined parameter  $\Lambda_c S^\alpha Re^\beta$

unifies the regime boundary, (ii) phase portrait analysis for hysteresis detection through forward and backward  $\Lambda$  ramps, and (iii) comparison with DNS results at selected  $(Re, S, \Lambda)$  points to assess the fidelity of the algebraic closure near the bifurcation.

#### DATA AVAILABILITY

All simulation code and data are publicly available at <https://github.com/slink/laminarization-transition-study>.

<sup>1</sup>J. C. Winterwerp, Journal of Geophysical Research: Oceans **106**, 22559 (2001).

<sup>2</sup>C. E. Ozdemir, T.-J. Hsu, and S. Balachandar, Journal of Fluid Mechanics **665**, 1 (2010).

<sup>3</sup>M. P. Lamb, E. A. D'Asaro, and J. D. Parsons, Journal of Geophysical Research: Oceans **109**, C12026 (2004).

<sup>4</sup>M. I. Cantero, S. Balachandar, and G. Parker, Journal of Turbulence **10**, N27 (2009).

<sup>5</sup>G. G. Stokes, Transactions of the Cambridge Philosophical Society **9**, 8 (1851).

<sup>6</sup>H. Schlichting and K. Gersten, *Boundary-Layer Theory*, 9th ed. (Springer, Berlin, 2017).

<sup>7</sup>C. von Kerczek and S. H. Davis, Journal of Fluid Mechanics **62**, 753 (1974).

<sup>8</sup>M. Hino, M. Sawamoto, and S. Takasu, Journal of Fluid Mechanics **75**, 193 (1976).

<sup>9</sup>M. Hino, M. Kashiyawanagi, A. Nakayama, and T. Hara, Journal of Fluid Mechanics **131**, 363 (1983).

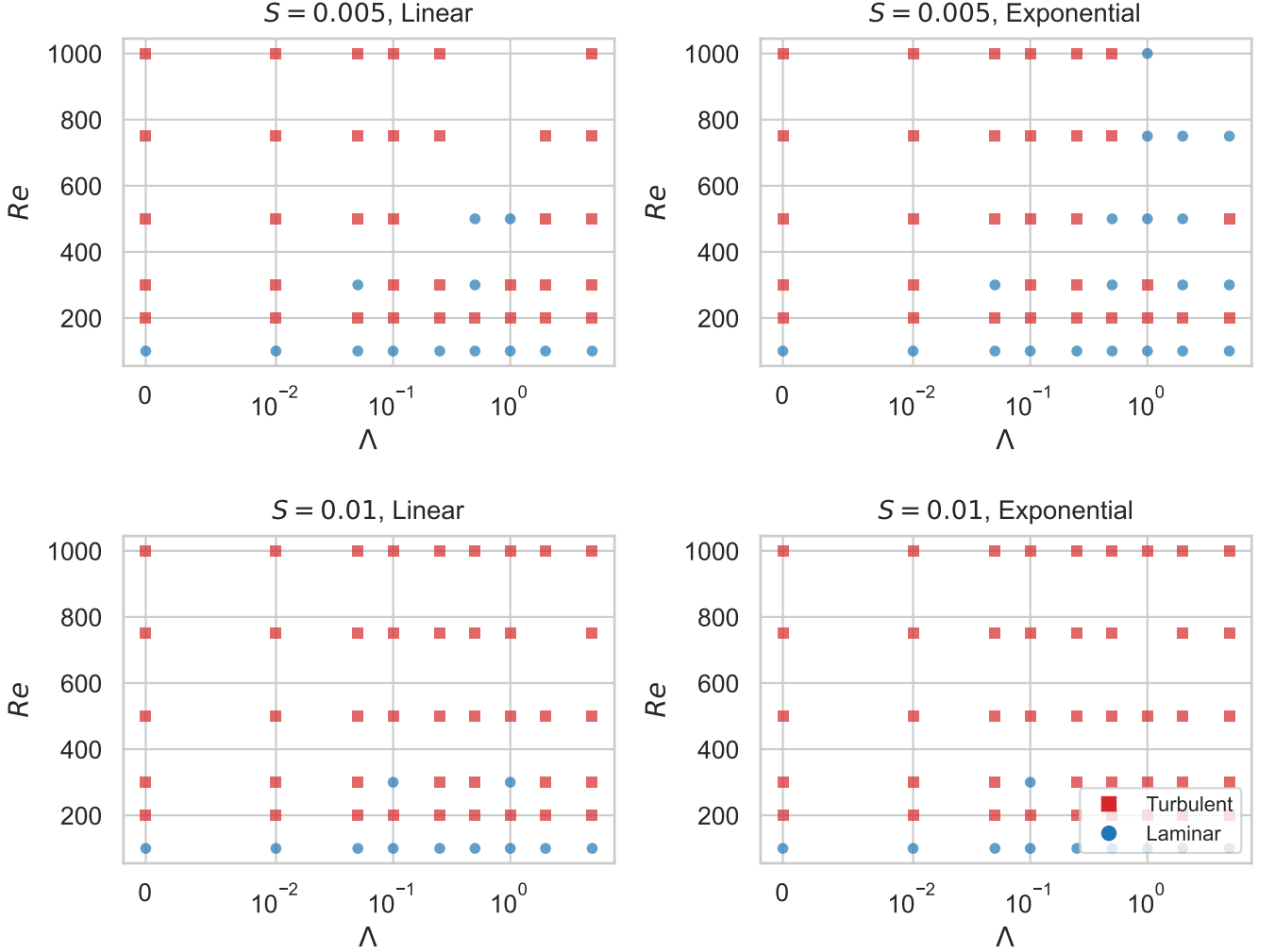


FIG. 8: Regime classification on the  $(\Lambda, Re_\delta)$  plane for linear damping (left) and exponential damping (right) at  $S = 0.005$  (top) and  $S = 0.01$  (bottom). Red squares: turbulent; blue circles: laminar. The transition boundary shifts to moderately higher  $\Lambda$  with exponential damping, but the qualitative topology is preserved.

- <sup>10</sup>R. Akhavan, R. D. Kamm, and A. H. Shapiro, *Journal of Fluid Mechanics* **225**, 395 (1991).
- <sup>11</sup>R. Akhavan, R. D. Kamm, and A. H. Shapiro, *Journal of Fluid Mechanics* **225**, 423 (1991).
- <sup>12</sup>B. L. Jensen, B. M. Sumer, and J. Fredsøe, *Journal of Fluid Mechanics* **206**, 265 (1989).
- <sup>13</sup>J. F. A. Sleath, *Journal of Fluid Mechanics* **182**, 369 (1987).
- <sup>14</sup>I. G. Jonsson, *Coastal Engineering Proceedings* **1**, 127 (1966).
- <sup>15</sup>W. D. Grant and O. S. Madsen, *Journal of Geophysical Research: Oceans* **84**, 1797 (1979).
- <sup>16</sup>J. Fredsøe and R. Deigaard, *Mechanics of Coastal Sediment Transport* (World Scientific, Singapore, 1992).
- <sup>17</sup>P. Nielsen, *Coastal Bottom Boundary Layers and Sediment Transport* (World Scientific, Singapore, 1992).
- <sup>18</sup>P. R. Spalart and B. S. Baldwin, *Turbulent Shear Flows* **6**, 417 (1989).
- <sup>19</sup>G. Vittori and R. Verzicco, *Journal of Fluid Mechanics* **371**, 207 (1998).
- <sup>20</sup>P. Costamagna, G. Vittori, and P. Blondeaux, *Journal of Fluid Mechanics* **474**, 1 (2003).
- <sup>21</sup>S. Salon, V. Armenio, and A. Crise, *Journal of Fluid Mechanics* **570**, 253 (2007).
- <sup>22</sup>P. Scandura, *Journal of Fluid Mechanics* **571**, 265 (2007).
- <sup>23</sup>C. E. Özdemir, T.-J. Hsu, and S. Balachandar, *Physics of Fluids* **26**, 045108 (2014).
- <sup>24</sup>S. Carstensen, B. M. Sumer, and J. Fredsøe, *Journal of Fluid Mechanics* **646**, 169 (2010).
- <sup>25</sup>S. Carstensen, B. M. Sumer, and J. Fredsøe, *Physics of Fluids* **24**, 115104 (2012).
- <sup>26</sup>J. M. Mier, J. M. Vetter, S. J. Gould, B. M. Sumer, and J. Fredsøe, *Journal of Fluid Mechanics* **910**, A17 (2021).
- <sup>27</sup>J. W. Miles, *Journal of Fluid Mechanics* **10**, 496 (1961).
- <sup>28</sup>L. N. Howard, *Journal of Fluid Mechanics* **10**, 509 (1961).
- <sup>29</sup>J. S. Turner, *Buoyancy Effects in Fluids* (Cambridge University Press, Cambridge, 1973).
- <sup>30</sup>G. N. Ivey, K. B. Winters, and J. R. Koseff, *Annual Review of Fluid Mechanics* **40**, 169 (2008).
- <sup>31</sup>J. H. Trowbridge and G. C. Kineke, *Journal of Geophysical Research: Oceans* **99**, 865 (1994).
- <sup>32</sup>C. T. Friedrichs, L. D. Wright, D. A. Hepworth, and S. C. Kim, *Continental Shelf Research* **20**, 807 (2000).
- <sup>33</sup>L. D. Wright and C. T. Friedrichs, *Continental Shelf Research* **26**, 2092 (2006).
- <sup>34</sup>J. C. Winterwerp, *Journal of Geophysical Research: Oceans* **111**, C05012 (2006).

- <sup>35</sup>C. M. Dohmen-Janssen, *Grain Size Influence on Sediment Transport in Oscillatory Sheet Flow*, Ph.D. thesis, Delft University of Technology (1999).
- <sup>36</sup>C. M. Dohmen-Janssen, D. F. Kroekenstiel, W. N. Hassan, and J. S. Ribberink, *Coastal Engineering* **46**, 61 (2002).
- <sup>37</sup>M. I. Cantero, M. Shringarpure, and S. Balachandar, *Geophysical Research Letters* **39**, L14603 (2012).
- <sup>38</sup>R. Narasimha and K. R. Sreenivasan, *Advances in Applied Mechanics* **19**, 221 (1979).
- <sup>39</sup>D. Greenblatt and E. A. Moss, *Journal of Fluid Mechanics* **514**, 65 (2004).
- <sup>40</sup>S. He and M. Seddighi, *Journal of Fluid Mechanics* **715**, 60 (2013).
- <sup>41</sup>O. Flores and J. J. Riley, *Boundary-Layer Meteorology* **139**, 241 (2011).
- <sup>42</sup>S. Balachandar and J. K. Eaton, *Annual Review of Fluid Mechanics* **42**, 111 (2010).
- <sup>43</sup>L. Prandtl, *Zeitschrift für Angewandte Mathematik und Mechanik* **5**, 136 (1925).
- <sup>44</sup>E. R. Van Driest, *Journal of the Aeronautical Sciences* **23**, 1007 (1956).
- <sup>45</sup>B. E. Launder and D. B. Spalding, *Computer Methods in Applied Mechanics and Engineering* **3**, 269 (1974).
- <sup>46</sup>D. C. Wilcox, *AIAA Journal* **26**, 1299 (1988).
- <sup>47</sup>G. L. Mellor and T. Yamada, *Journal of the Atmospheric Sciences* **31**, 1791 (1974).
- <sup>48</sup>G. L. Mellor and T. Yamada, *Reviews of Geophysics* **20**, 851 (1982).
- <sup>49</sup>W. Rodi, *Journal of Geophysical Research: Oceans* **92**, 5305 (1987).
- <sup>50</sup>S. B. Pope, *Turbulent Flows* (Cambridge University Press, Cambridge, 2000).
- <sup>51</sup>W. H. Munk and E. R. Anderson, *Journal of Marine Research* **7**, 276 (1948).
- <sup>52</sup>V. Armenio and S. Sarkar, *Journal of Fluid Mechanics* **459**, 1 (2002).
- <sup>53</sup>J. R. Taylor, S. Sarkar, and V. Armenio, *Physics of Fluids* **17**, 116602 (2005).
- <sup>54</sup>J. R. Taylor and S. Sarkar, *Journal of Physical Oceanography* **38**, 2535 (2008).
- <sup>55</sup>G. Brethouwer, P. Billant, E. Lindborg, and J.-M. Chomaz, *Journal of Fluid Mechanics* **585**, 343 (2007).
- <sup>56</sup>F. Zonta, M. Onorato, and A. Soldati, *Journal of Fluid Mechanics* **697**, 175 (2012).
- <sup>57</sup>B. D. Mater and S. K. Venayagamoorthy, *Physics of Fluids* **26**, 036601 (2014).
- <sup>58</sup>T. R. Osborn, *Journal of Physical Oceanography* **10**, 83 (1980).